

Truly chiral phonons in α -HgS observed by circularly polarised Raman spectroscopy

Kyosuke Ishito^{1#}, Huiling Mao^{1#}, Yusuke Kousaka^{2,3}, Yoshihiko Togawa², Satoshi Iwasaki³, Tiantian Zhang^{1,4}, Shuichi Murakami^{1,4}, Jun-ichiro Kishine^{5,6} & Takuya Satoh^{1*}

¹*Department of Physics, Tokyo Institute of Technology, Tokyo 152-8551, Japan*

²*Department of Physics and Electronics, Osaka Prefecture University, Osaka 599-8531, Japan*

³*Research Institute for Interdisciplinary Science, Okayama University, Okayama 700-8530, Japan*

⁴*Tokodai Institute for Element Strategy (TIES), Tokyo Institute of Technology, Tokyo 152-8551, Japan*

⁵*Division of Natural and Environmental Sciences, The Open University of Japan, Chiba 261-8586, Japan*

⁶*Institute for Molecular Science, Okazaki, Aichi 444-8585, Japan*

#*These authors contributed equally to this work*

**e-mail: satoh@phys.titech.ac.jp*

Chirality is a manifestation of the asymmetry inherent in nature. Chirality has been defined as the symmetry breaking of the parity of static objects¹, and the definition was extended to dynamic motion such that true and false chiralities were distinguished². Recently, rotating, yet not propagating, atomic motions were predicted and observed in two-dimensional materials, and they were referred to as ‘chiral phonons’³⁻⁵. A natural development would be the discovery of truly chiral phonons that propagate while rotating in three-dimensional materials. Here, we used circularly polarised Raman scattering and first-principles calculations to identify truly chiral phonons in chiral bulk crystals. This approach enabled us to determine the chirality of a crystal in a noncontact and nondestructive manner. In addition, we demonstrated that the law of the conservation of pseudoangular momentum holds between circularly polarised photons and chiral phonons. These findings are foreseen to pave the way for transferring the pseudoangular momentum from photons to electron spins via the

propagating chiral phonons in opto-phononic-spintronic devices.

Chirality, the breaking of reflection and inversion symmetries¹, appears at all levels of nature and has been studied in many fields of research⁶. Barron extended the concept of chirality to the dynamic regime as classified into *true* and *false* chiralities². True chirality is demonstrated by systems that exist in two different enantiomeric states that are interconverted by spatial inversion (\mathcal{P}), rather than by time inversion (\mathcal{T}) combined with appropriate spatial rotation (\mathcal{R})². This concept contrasts with false chirality, where the two states are interconverted by \mathcal{P} and by \mathcal{T} ; for example, the magneto-optical Faraday rotation.

Chirality was further extended to the dynamics of quasi-particles. Possible band-structure shapes have been classified in terms of pseudomomentum and pseudoangular momentum (PAM)⁷, which originate from the phase factors acquired by discrete translation and rotation symmetry operations on wave functions, respectively. In crystals, they are different from the momentum and angular momentum (AM), which are continuous linear and circular motions of an object in real space, respectively. Recently, circularly rotating, yet not propagating, atomic motion with nonzero PAM and AM at high symmetry points in the Brillouin zone in monolayer hexagonal lattices was theoretically predicted and named ‘chiral phonons’^{3,4}. This prediction was experimentally verified in the transition metal dichalcogenide WSe₂ via transient infrared (IR) spectroscopy⁵.

Employing Barron’s true chirality, one can extend the concept of a chiral phonon to ‘truly chiral phonons’, which have two enantiomeric chiral modes that propagate while circularly rotating in three-dimensional materials with opposite signs of PAM and AM. These modes should be interconverted by \mathcal{P} , but not by \mathcal{RT} . The observation of truly chiral phonons would require the use of chiral materials, as has been proposed theoretically⁸. Several Raman experiments designed to identify phonon symmetry in chiral crystals were conducted⁹⁻¹⁵. Frequency-degenerated phonon modes were observed to undergo splitting at the centre of the Brillouin zone (Γ_3 doublets) in α -quartz and trigonal tellurium^{9,11}. Moreover, theoretical work on phonon band dispersion has been reported on α -HgS (cinnabar), where the splitting was attributed to the linear wave-vector

shifts caused by chirality¹⁶. Nonetheless, previous studies have mostly focused on examining the phonon symmetry without considering PAM and AM.

Here, we used circularly polarised Raman spectroscopy (see Methods) to observe the phonon modes and their splitting in chiral crystals of α -HgS. Moreover, we performed first-principles calculations (see Methods) to compute the dispersion, PAM, and AM of phonons in α -HgS. A comparison between the experiment and calculation shows that the split phonons were indeed truly chiral phonons. We also confirmed that the conservation law of PAM holds in circularly polarised Raman scattering by taking into account the three-fold rotational symmetry.

Trigonal α -HgS crystals contain two enantiomeric cinnabar structures with right- and left-handed helices (R- and L-HgS), which belong to the space groups $P3_121$ and $P3_221$, respectively¹⁷. This crystal has a three-fold helical axis along the c -direction (Fig. 1(a)), with large optical activity¹⁸. Our samples were single crystals of naturally grown α -HgS with lateral dimensions of 3 mm. We selected a c -axis-oriented as-grown surface of R-HgS, which was confirmed by X-ray analysis.

The phonon modes at the centre of the Brillouin zone (Γ point) of α -HgS are classified into two $\Gamma_1^{(1,2)}$ singlets (Raman active), three $\Gamma_2^{(1-3)}$ singlets (IR active), and five $\Gamma_3^{(1-5)}$ doublets (Raman and IR active). Our measurement led to the observation of the $\Gamma_1^{(1,2)}$ and $\Gamma_3^{(2-5)}$ doublets, which were assigned on the basis of the selection rule¹⁹ for the four incident/scattered polarisation configurations (RR, LL, RL, and LR), where $I_{RR} : I_{LL} : I_{RL} : I_{LR} = 1 : 1 : 0 : 0$ and $0 : 0 : 1 : 1$ for the Γ_1 and Γ_3 modes, respectively (Extended Data Fig. 1). The transverse optical (TO) phonons of the Γ_3 mode were generated because the incident and scattered light were propagated along the c -axis. A weak signal was detected for the longitudinal optical (LO) phonon at $\sim 145 \text{ cm}^{-1}$, presumably due to misalignment of the experimental setup.

The phonon frequencies obtained by the Raman experiment are compared with the results of the first-principles calculations and with previous results^{10,16} in Extended Data Table 1. The

results of the Raman experiments both in our study and in a previous study¹⁰ are identical to within 3 cm^{-1} . The results of our calculations at the Γ point also closely approximate those in Ref.¹⁶, and the small differences are attributed to the difference in the positions of the atoms. In our experiments, the $\Gamma_3^{(1)}$ mode was not observed because this mode is nearly degenerate with the $\Gamma_1^{(1)}$ mode, which has a much higher intensity. In Extended Data Table 1, the frequencies of the $\Gamma_3^{(2-5)}$ modes obtained in our Raman experiment are averaged for the RL and LR configurations, which were split as shown in the next paragraph.

The Stokes and anti-Stokes Raman spectra (Raman optical activity) of each $\Gamma_3^{(2-5)}$ mode are shown in Figs. 2(a–h). All four Γ_3 modes were observed with the opposite circularly polarised light between the incident and scattered light (RL and LR). On the anti-Stokes spectra [see Figs. 2(a–d)], the absolute values of the Raman shift of the $\Gamma_3^{(2)}$ and $\Gamma_3^{(4)}$ modes in the RL configuration are lower than those in the LR configuration in Figs. 2(a) and (c). In Figs. 2(b) and (d), the absolute values of the Raman shift of the $\Gamma_3^{(3)}$ and $\Gamma_3^{(5)}$ modes in the RL configuration are higher than those in the LR configuration. On the Stokes spectra [see Figs. 2(e–h)], the splittings are mirror images of those on the anti-Stokes spectra [see Figs. 2(a–d)]. The $\Gamma_1^{(1,2)}$ modes do not split.

The properties of phonons are discussed here on the basis of our first-principles calculations. Figure 3(a) displays the phonon dispersion curve calculated along the path Δ from Γ to A point, which is parallel to the c -axis [see Fig. 1(b)]. Linear splittings of $\Gamma_3^{(1-5)}$ modes appear around the Γ point, which is consistent with previous calculations^{16,20}. From the conservation law of pseudomomentum, the wavenumber k of phonons observed by backscattering Raman spectroscopy is expressed as $k = 4\pi n/\lambda$, where λ is the wavelength of the incident or scattered light, $n = 2.77$ is the absolute value of the complex refractive index of α -HgS²¹. The value of k was calculated to be $\sim 1/80$ of the wavenumber π/c at the A point. We denoted this specific point on the path Δ as ‘N’ in Fig. 3(a). The experimental splitting values of the Γ_3 modes at this point (Stokes scattering) are almost consistent with the calculations, as indicated in Extended Data Table 2. Therefore, we attribute the observed splittings in Fig. 2 to the linear k shifts at the N point.

To understand the selection rule of the incident/scattered polarisation configurations on the Raman spectra in Fig. 2, we calculated the PAM of phonons in R-HgS (see Methods). As shown in Fig. 3(a), the Γ_3 doublets have spin PAM $l_{\text{PAM}}^s = \pm 1$, whereas the Γ_1 and Γ_2 singlets have $l_{\text{PAM}}^s = 0$. The phonon bands with $l_{\text{PAM}}^s = -1$ and $l_{\text{PAM}}^s = 0$ intersect at the A point. These are the common features of the 3_1 (right-handed) helix^{7,9,22}. From Figs. 2(e–h) and 3(a), $\Gamma_3^{(2-5)}$ phonons with $l_{\text{PAM}}^s = +1$ and -1 were observed in the LR and RL configurations, respectively (Extended Data Table 2). Γ_1 phonons with $l_{\text{PAM}}^s = 0$ were observed in the RR and LL configurations. Right- and left-handed circularly polarised light possess PAM of $\sigma = +1$ and -1 , respectively²³. Therefore, we confirmed a conservation law to exist between the spin PAM of phonons and the PAM of the incident/scattered photons in the Stokes spectra as

$$\sigma_s - \sigma_i = -l_{\text{PAM}}^s + 3p, \quad (1)$$

where σ_s and σ_i represent the PAM of the scattered and incident photons, respectively. In addition, $p = 0$ and ± 1 for the Γ_1 and Γ_3 modes, respectively. The factor $3p$ on the right-hand side of equation (1) can be understood by considering the three-fold rotational symmetry of α -HgS and the Umklapp process in Raman scattering^{7,24–27}.

In crystals with discrete rotational symmetry, the PAM and AM of phonons should be distinguished. The AM of phonons arises from the circular vibration of atoms in the real space, as shown in Figs. 1(c–f) [See also Supplementary Movies 1 and 2]. The AM of phonons along the c -axis is displayed in Fig. 3(b) along with Γ to A point (see Methods). In the vicinity of the Γ point, the Γ_3 modes have clockwise and counter clockwise rotations, corresponding to the positive and negative AM of phonons, respectively. This is a clear manifestation of the existence of chiral phonons. The Γ_1 modes have linear vibrations with zero AM of phonons. The signs of AM at the N point are listed in Extended Data Table 2, where the spin PAM and AM of phonons do not correspond with each other. This indicates that, contrary to PAM, the AM of phonons is not conserved during the Raman process.

We also calculated the PAM and AM of phonons in L-HgS (Extended Data Fig. 2). The signs

of spin PAM and AM are reversed with respect to Fig. 3, that is, $l_{\text{PAM}}^s(\text{RH}, k, j) = -l_{\text{PAM}}^s(\text{LH}, k, j)$ and $l_{\text{AM}}(\text{RH}, k, j) = -l_{\text{AM}}(\text{LH}, k, j)$, where RH and LH denote crystals with right- and left-handed helices, respectively. This means that the splitting of the Γ_3 modes arises from chirality. From the first-principles calculation, the phonon eigenvector at the N point $\mathbf{u}(\text{RH}, k, j)$ and $\mathbf{u}(\text{LH}, k, j)$ are converted by \mathcal{P} , \mathcal{T} , and \mathcal{C}_2 as $\mathcal{P}\mathbf{u}(\text{RH}, k, j) = \mathbf{u}(\text{LH}, -k, j)$, $\mathcal{C}_2\mathcal{T}\mathbf{u}(\text{RH}, k, j) = \mathcal{C}_2\mathbf{u}(\text{RH}, -k, j) = \mathbf{u}(\text{RH}, k, j)$, where \mathcal{C}_2 is a two-fold rotation around the \mathbf{a} , \mathbf{b} , or $\mathbf{a} + \mathbf{b}$ direction. These relations satisfy the definition of true chirality with two different enantiomeric phonon modes: $\mathbf{u}(\text{RH}, k, j)$ and $\mathbf{u}(\text{LH}, -k, j)$.

We also recorded the Raman spectra of an α -HgS crystal for which the handedness (chirality) of the measured region was unknown because the size of the chiral domain was smaller than the experimental resolution (~ 1 mm) of our X-ray diffractometer. Contrary to the X-ray analysis, our Raman experiment with a spatial resolution of a few μm succeeded in observing the splitting of the Γ_3 modes (Extended Data Fig. 3), and the directions of the splittings were opposite to the results in Fig. 2. Considering the data in Extended Data Table 3, the chirality of the sample was found to be left-handed.

The space group analysis enabled us to additionally assign an irreducible representation of the phonon dispersion curve in R-HgS. On path Δ from Γ to A, three irreducible representations are known to exist: Δ_1 , Δ_2 , and Δ_3 ^{20,28}. The labels of the irreducible representations are based on the convention in Ref. ²⁸. The Γ_1 and Γ_2 modes at the Γ point change to the Δ_1 mode, whereas the Γ_3 modes split into Δ_2 and Δ_3 modes in accordance with the compatibility relations. In the Supplementary Information, we present a derivation of the Raman tensors that correspond to the Δ_2 and Δ_3 modes. It follows that the Raman intensities of the Δ_2 and Δ_3 modes are $I_{\text{RR}} : I_{\text{LL}} : I_{\text{RL}} : I_{\text{LR}} = 0 : 0 : 1 : 0$ and $0 : 0 : 0 : 1$, respectively. This is consistent with the results of the Raman experiments. In other words, spin PAM $l_{\text{PAM}}^s(\text{RH}) = 0, +1, -1$ correspond to $\Delta_1, \Delta_2, \Delta_3$, respectively, because the phase change by three-fold rotation is the index of each irreducible representation. For L-HgS, $l_{\text{PAM}}^s(\text{LH}) = 0, +1, -1$ correspond to $\Delta_1, \Delta_3, \Delta_2$, respectively²⁸.

Next, we discuss the propagation of the chiral phonons. From Fig. 3, the group velocities of the $\Gamma_3^{(1-5)}$ modes at the N point are calculated as $\sim \pm 0.4-2 \times 10^3$ m/s, which is comparable to the sound velocity of acoustic phonons. Note that the nonreciprocal propagation of chiral phonons can be controlled by the PAM of the photon. This implies the possibility of transferring the PAM from photons to electron spins via the propagating chiral phonons in opto-phononic-spintronic devices.

Weyl phonons can exist widely in chiral crystals, which have been predicted by the first-principles calculations and verified by inelastic X-ray scattering^{29,30}. We note that circularly polarized Raman spectroscopy presented in this paper may open the possibility to detect phonons carrying nonzero Chern number through measuring the phonon PAM, instead of detecting the eigenvalue and eigenvectors of the topological bands.

We observed chiral phonons in a three-dimensional chiral system using circularly polarised Raman spectroscopy and first-principles calculations. The chiral phonons were labelled with spin PAM of $\{+1, -1\}$ corresponding to $\{\Delta_2, \Delta_3\}$ and $\{\Delta_3, \Delta_2\}$ for R- and L-HgS, respectively, with opposite group velocities of ~ 1 km/s. The parity and time-reversal symmetries of the phonons satisfy the definition of truly chiral phonons, which propagate while rotating along the c -axis. This is distinct from the chiral phonons observed in two-dimensional hexagonal systems. Our work also provides an optical method to identify the handedness of chiral materials using PAM and we demonstrated that the spatial imaging of chiral domains can be achieved in a noncontact and nondestructive manner.

Data availability The data that support the findings of this study are available from the corresponding author upon reasonable request.

References

1. Kelvin, W. T. B. *Baltimore Lectures on Molecular Dynamics and the Wave Theory of Light* (Cambridge University Press, 1904).

2. Barron, L. D. *Molecular Light Scattering and Optical Activity*, 2nd ed. (Cambridge University Press, 2004).
3. Zhang, L. & Niu, Q. Chiral phonons at high-symmetry points in monolayer hexagonal lattices. *Phys. Rev. Lett.* **115**, 115502 (2015).
4. Chen, H., Zhang, W., Niu, Q. & Zhang, L. Chiral phonons in two-dimensional materials. *2D Materials* **6**, 012002 (2019).
5. Zhu, H. et al. Observation of chiral phonons. *Science* **359**, 579–582 (2018).
6. Cahn, R. S., Ingold, C., & Prelog, V. Specification of molecular chirality. *Angew. Chem. Int. Ed. Engl.* **5**, 385–415 (1966).
7. Božovic, I. Possible band-structure shapes of quasi-one-dimensional solids. *Phys. Rev. B* **29**, 6586–6599 (1984).
8. Kishine, J., Ovchinnikov, A. S. & Tereshchenko, A. A. Chirality-induced phonon dispersion in a noncentrosymmetric micropolar crystal. *Phys. Rev. Lett.* **125**, 245302 (2020).
9. Pine, A. S. & Dresselhaus, G. Linear wave-vector shifts in the Raman spectrum of α -quartz and infrared optical activity. *Phys. Rev.* **188**, 1489–1496 (1969).
10. Zallen, R., Lucovsky, G., Taylor, W., Pinczuk, A. & Burstein, E. Lattice vibrations in trigonal HgS. *Phys. Rev. B* **1**, 4058–4070 (1970).
11. Pine, A. S. & Dresselhaus, G. Raman spectra and lattice dynamics of tellurium. *Phys. Rev. B* **4**, 356–371 (1971).
12. Grimsditch, M. H., Ramdas, A. K., Rodriguez, S. & Tekippe, V. J. Piezospectroscopy of Raman lines exhibiting linear wave-vector dependence: α -quartz. *Phys. Rev. B* **15**, 5869–5876 (1977).
13. Imaino, W., Simpson, C. T., Becker, W. M. & Ramdas, A. K. Resonant Raman effect in cinnabar. *Phys. Rev. B* **21**, 634–642 (1980).

14. Garasevich, S. G., Slobodyanyuk, A. V. & Yanchuk, Z. Z. Anomalous angular dependence of E-mode splitting in Raman spectra of ZnP_2 and CdP_2 uniaxial gyrotropic crystals caused by spatial dispersion. *Phys. Lett. A* **197**, 238–242 (1995).
15. Pinan-Lucarre, J.-P., Ouillon, R. & Ranson, P. Linear wave vector dependence of low-frequency Raman modes in two uniaxial gyrotropic quartz-type materials: α - GaPO_4 and α - AlPO_4 . *Chem. Phys. Lett.* **302**, 164–170 (1999).
16. Cardona, M. et al. Electronic and phononic properties of cinnabar: Ab initio calculations and some experimental results. *Phys. Rev. B* **82**, 085210 (2010).
17. Aurivillius, K. L. On the crystal structure of cinnabar. *Acta. Chem. Scand.* **4**, 1413–1436 (1950).
18. Glazer, A. M., Stadnicka, K. On the origin of optical activity in crystal structures. *J. Appl. Cryst.* **19**, 108–122 (1986).
19. Higgs, P. W. The vibration spectra of helical molecules: infra-red and Raman selection rules, intensities and approximate frequencies. *Proc. Math. Phys. Eng. Sci.* **220**, 472–485 (1953).
20. Nusimovici, M. A. & Gorre, G. Phonons in cinnabar. *Phys. Rev. B* **8**, 1648–1656 (1973).
21. Bond, W. L., Boyd, G. D. & Carter Jr., H. L. Refractive indices of HgS (cinnabar) between 0.62 and 11 μ . *J. Appl. Phys.* **38**, 4090–4091 (1967).
22. Nussbaum, A. & Hager, R. J. Galvanomagnetic coefficients of single-crystal tellurium. *Phys. Rev.* **123**, 1958–1964 (1961).
23. Yariv, A. & Yeh, P. *Photonics: Optical Electronics in Modern Communications*, 6th. ed. (Oxford University Press, New York, 2006).
24. Bloembergen, N. Conservation laws in nonlinear optics. *J. Opt. Soc. Am.* **70**, 1429–1436 (1980).

25. Tatsumi, Y., Kaneko, T. & Saito, R. Conservation law of angular momentum in helicity-dependent Raman and Rayleigh scattering. *Phys. Rev. B* **97**, 195444 (2018).
26. Chen, H., Wu, W., Zhu, J., Yang, S. A. & Zhang, L. Propagating chiral phonons in three-dimensional materials. *Nano Lett.* **21**, 3060–3065 (2021).
27. Zhang, T. & Murakami, S. Chiral phonons and pseudo-angular momentum in non-symmorphic systems. *arXiv:2107.04243v1* (2021).
28. Teuchert, W. D. & Geick, R. Symmetry of lattice vibrations in selenium and tellurium. *Phys. Stat. Sol. B* **61**, 123–136 (1974).
29. Zhang, T. et al. Double-Weyl phonons in transition-metal monosilicides. *Phys. Rev. Lett.* **120**, 016401 (2018).
30. Li, H. et al. Observation of a chiral wave function in the twofold-degenerate quadruple Weyl system BaPtGe. *Phys. Rev. B* **103**, 184301 (2021).

Acknowledgments

We would like to thank M. Kichise, A. Kawano, K. Matsumoto, A. Koreeda, Y. Fujii, E. Oishi, and H. M. Yamamoto for their valuable discussions and technical support. T.S. was financially supported by the Japan Society for the Promotion of Science (JSPS) KAKENHI (Grant No. JP19H01828, No. JP19H05618, No. JP19K21854, No. JP21H01032), and the Frontier Photonic Sciences Project of the National Institutes of Natural Sciences (NINS) (Grant Nos. 01212002 and 01213004).

Author contributions

T.S. and J.K. conceived the study. K.I. and H.M. performed the Raman experiments. Y.K., Y.T., and S.I. conducted the X-ray analyses. K.I., H.M., T.Z., and S.M. performed the first-principles calculations. K.I., M.H., J.K., and T.S. wrote the manuscript. All authors discussed the results and commented on the manuscript.

Competing interests

The authors declare no competing interests.

Methods

Raman scattering. We used a custom-built Raman spectroscopy system equipped with a monochromator, charge-coupled device (CCD) camera, and optical elements. Details of the setup can be found elsewhere³¹. Excitation light was generated by a diode laser with a wavelength of $\lambda = 785$ nm. The incident and scattered light were propagated along the c -axis of the crystal. All the measurements were performed at room temperature.

First-principles calculation. First-principles calculations were performed using the ABINIT package^{32,33} which implements the density functional perturbation theory (DFPT)³⁴. An anadbb was used to obtain the phonon dispersion curve^{35,36}. For the calculation of phonon dispersion, the exchange-correlation energy of electrons is described as the generalized gradient approximation (GGA) with the norm-conserving pseudopotentials^{37,38}, and spin-orbit coupling was not considered. We set the kinetic-energy cutoff to 60 Ha, which was necessary to obtain a well-converged result, and the grids of the wave vector k $6 \times 6 \times 4$ to describe the phonon dispersion curve. In addition, we increased the precision of the k grids to $8 \times 8 \times 8$ to obtain the converged phonon frequency at the Γ point. The lattice parameters of α -HgS were used as follows: volume of the cell $V_0 = 160.02 \text{ \AA}^3$, and the length of the cell is $a = 4.11 \text{ \AA}$, $b = 4.11 \text{ \AA}$, and $c = 9.40 \text{ \AA}$, the angle of cell $\alpha = 90^\circ$, $\beta = 90^\circ$, and $\gamma = 120^\circ$ ^{39,40}. The essential part of the ABINIT results was confirmed using the VASP package.

Calculation of PAM. In a material with three-fold rotational symmetry, PAM has been defined as follows^{3,7}

$$\{C_3 | 0\} \mathbf{u}(\mathbf{k}) = \exp \left[-i \frac{2\pi}{3} l_{\text{PAM}}(\mathbf{k}) \right] \mathbf{u}(\mathbf{k}), \quad (2)$$

where $l_{\text{PAM}}(\mathbf{k})$ is the PAM of phonons, $\mathbf{u}(\mathbf{k})$ is the displacement vector, and $\{C_3 | 0\}$ is the three-

fold rotation around the c -axis. However, α -HgS has a three-fold helical rotational symmetry instead of a three-fold rotational symmetry. Therefore, we defined the PAM of phonons in R- and L-HgS as follows²⁷:

$$\{C_3 | \mathbf{c}/3\} \mathbf{u}(\text{RH}, \mathbf{k}) = \exp \left[-i \frac{2\pi}{3} l_{\text{PAM}}(\text{RH}, \mathbf{k}) \right] \mathbf{u}(\text{RH}, \mathbf{k}), \quad (3)$$

$$\{C_3 | 2\mathbf{c}/3\} \mathbf{u}(\text{LH}, \mathbf{k}) = \exp \left[-i \frac{2\pi}{3} l_{\text{PAM}}(\text{LH}, \mathbf{k}) \right] \mathbf{u}(\text{LH}, \mathbf{k}), \quad (4)$$

where $\{C_3 | \mathbf{c}/3\}$ and $\{C_3 | 2\mathbf{c}/3\}$ are combinations of the three-fold rotation around the c -axis and the $c/3$ and $2c/3$ translations along the c -axis, respectively.

The displacement vector of phonons can be expressed as follows

$$\mathbf{u}_\kappa(\mathbf{k}, l, j) = m_\kappa^{-\frac{1}{2}} \boldsymbol{\epsilon}_\kappa(\mathbf{k}, j) \exp [i \{ \mathbf{k} \cdot \mathbf{R}_l - \omega(\mathbf{k}, j)t \}], \quad (5)$$

where j is the number of phonon modes, m_κ is the mass of the κ -th atom in the l -th unit cell, $\boldsymbol{\epsilon}_\kappa(\mathbf{k}, j)$ is the eigenvector of the dynamical matrix, and \mathbf{R}_l is the position of the l -th unit cell. The use of equation (5) indicates that the phase of the eigenvector consists of two parts: $\boldsymbol{\epsilon}(\mathbf{k})$ and $\exp [i\mathbf{k} \cdot \mathbf{R}_l]$, both of which contribute to the calculation of the PAM. In the former, the phase difference of $\boldsymbol{\epsilon}(\mathbf{k})$ leads to the spin PAM l_{PAM}^s , which is quantized as an integer. The latter factor, $\exp [i\mathbf{k} \cdot \mathbf{R}_l]$ provides the orbital PAM l_{PAM}^o , which is therefore equal to $\frac{1}{2\pi} \mathbf{k} \cdot \mathbf{c}$ under a three-fold helical rotation. Consequently, for each wavenumber \mathbf{k} , the total PAM is

$$l_{\text{PAM}} = l_{\text{PAM}}^s + l_{\text{PAM}}^o. \quad (6)$$

Here, we considered only the spin PAM in the phonon dispersion, as shown in Fig. 5(a).

Calculation of AM. The AM of phonons at wavenumber \mathbf{k} of mode number j is defined as⁴¹

$$l_{\text{AM}}(\mathbf{k}, j) = (\boldsymbol{\epsilon}(\mathbf{k}, j)^\dagger M \boldsymbol{\epsilon}(\mathbf{k}, j)) \hbar. \quad (7)$$

where $M = \begin{pmatrix} 0 & -i & 0 \\ i & 0 & 0 \\ 0 & 0 & 0 \end{pmatrix} \otimes I_{n \times n}$, where n is the number of atoms in a unit cell and $I_{n \times n}$ is a

unit matrix of $n \times n$. The eigenvector of the dynamical matrix $\epsilon(\mathbf{k}, j)$ is normalised as:

$$\epsilon(\mathbf{k}, j)^\dagger \epsilon(\mathbf{k}, j) = 1. \quad (8)$$

The origin of spin and orbital PAMs. Here we provide an explicit form of the spin and orbital PAMs associated with the screw operation $\{C_3 | \mathbf{c}/3\}$, where $\mathbf{c}/3$ is the non-primitive translation. The atomic displacement amplitude associated with the phonon propagation may be generally written as

$$\mathbf{U}_{\mathbf{k}}(\mathbf{r}) = \epsilon(\mathbf{k}) \exp(i\mathbf{k} \cdot \mathbf{r}). \quad (9)$$

The vector field, $\mathbf{U}_{\mathbf{k}}(\mathbf{r})$, is then transformed in accordance with a general rule:

$$\{C_3 | \mathbf{c}/3\} \mathbf{U}_{\mathbf{k}}(\mathbf{r}) = [C_3 \epsilon(\mathbf{k})] \exp(i\mathbf{k} \cdot \{C_3 | \mathbf{c}/3\}^{-1} \mathbf{r}). \quad (10)$$

Note that $\{C_3 | \mathbf{c}/3\}^{-1} = \{C_3^{-1} | -C_3^{-1} \mathbf{c}/3\}$, $\mathbf{k} \cdot \mathbf{r}$ is a scalar, and $C_3 \epsilon(\mathbf{k}) = \exp(-i\frac{2\pi}{3}m) \epsilon(\mathbf{k})$, we have

$$\{C_3 | \mathbf{c}/3\} \mathbf{U}_{\mathbf{k}}(\mathbf{r}) = \exp\left[-i\frac{2\pi}{3}(l_{\text{PAM}}^s + l_{\text{PAM}}^o)\right] \mathbf{U}_{\mathbf{k}}(\mathbf{r}) \quad (11)$$

where the respective spin and orbital pseudoangular momenta are introduced by

$$l_{\text{PAM}}^s = m, \quad (12)$$

and

$$l_{\text{PAM}}^o = -\frac{3}{2\pi} \{(C_3 \mathbf{k}) - \mathbf{k}\} \cdot \mathbf{r} + \frac{1}{2\pi} (C_3 \mathbf{k}) \cdot \mathbf{c}, \quad (13)$$

which yield the total PAM, $l_{\text{PAM}} = l_{\text{PAM}}^s + l_{\text{PAM}}^o$.

In this study, we consider path Δ from Γ to A, where $C_3 \mathbf{k} = \mathbf{k}$ denotes the modulo reciprocal lattice vectors. Thus, $l_{\text{PAM}}^o = \frac{1}{2\pi} \mathbf{k} \cdot \mathbf{c}$. The same symmetry properties apply to the photons propagating along the helical axis. Then, we obtain the selection rule (1), which includes only l_{PAM}^s , by cancelling out the l_{PAM}^o terms because of the law of conservation of momentum.

References

31. Hsu, W.-H., Shen, K., Fujii, Y., Koreeda, A. & Satoh, T. Observation of terahertz magnon of Kaplan-Kittel exchange resonance in yttrium-iron garnet by Raman spectroscopy. *Phys. Rev. B* **102**, 174432 (2020).
32. Gonze, X. et al. ABINIT: First-principles approach to material and nanosystem properties. *Comput. Phys. Commun.* **180**, 2582–2615 (2009).
33. Romero, A. H. et al. ABINIT: Overview, and focus on selected capabilities. *J. Chem. Phys.* **152**, 124102 (2020).
34. Hamann, D. R., Wu, X., Rabe, K. M. & Vanderbilt, D. Metric tensor formulation of strain in density-functional perturbation theory. *Phys. Rev. B* **71**, 035117 (2005).
35. Gonze, X. First-principles responses of solids to atomic displacements and homogeneous electric fields: Implementation of a conjugate-gradient algorithm. *Phys. Rev. B* **55**, 10337–10354 (1997).
36. Gonze, X. & Lee, C. Dynamical matrices, Born effective charges, dielectric permittivity tensors, and interatomic force constants from density-functional perturbation theory. *Phys. Rev. B* **55**, 10355–10368 (1997).
37. van Setten, M. J. et al. The PseudoDojo: Training and grading a 85 element optimized norm-conserving pseudopotential table. *Comput. Phys. Commun.* **226**, 39–54 (2018).
38. Hamann, D. R. Optimized norm-conserving Vanderbilt pseudopotentials. *Phys. Rev. B* **88**, 085117 (2013).
39. Jain, A. et al. Commentary: The Materials project: A materials genome approach to accelerating materials innovation. *APL Mater.* **1**, 011002 (2013).
40. Rodic, D., Spasojevic, V., Bajorek, A. & Onnerud, P. Similarity of structure properties of $\text{Hg}_{1-x}\text{Mn}_x\text{S}$ and $\text{Cd}_{1-x}\text{Mn}_x\text{S}$ (structure properties of HgMnS and CdMnS). *J. Magn. Magn. Mater.* **152**, 159–164 (1996).

41. Zhang, L. & Niu, Q. Angular momentum of phonons and the Einstein–de Haas effect. *Phys. Rev. Lett.* **112**, 085503 (2014).

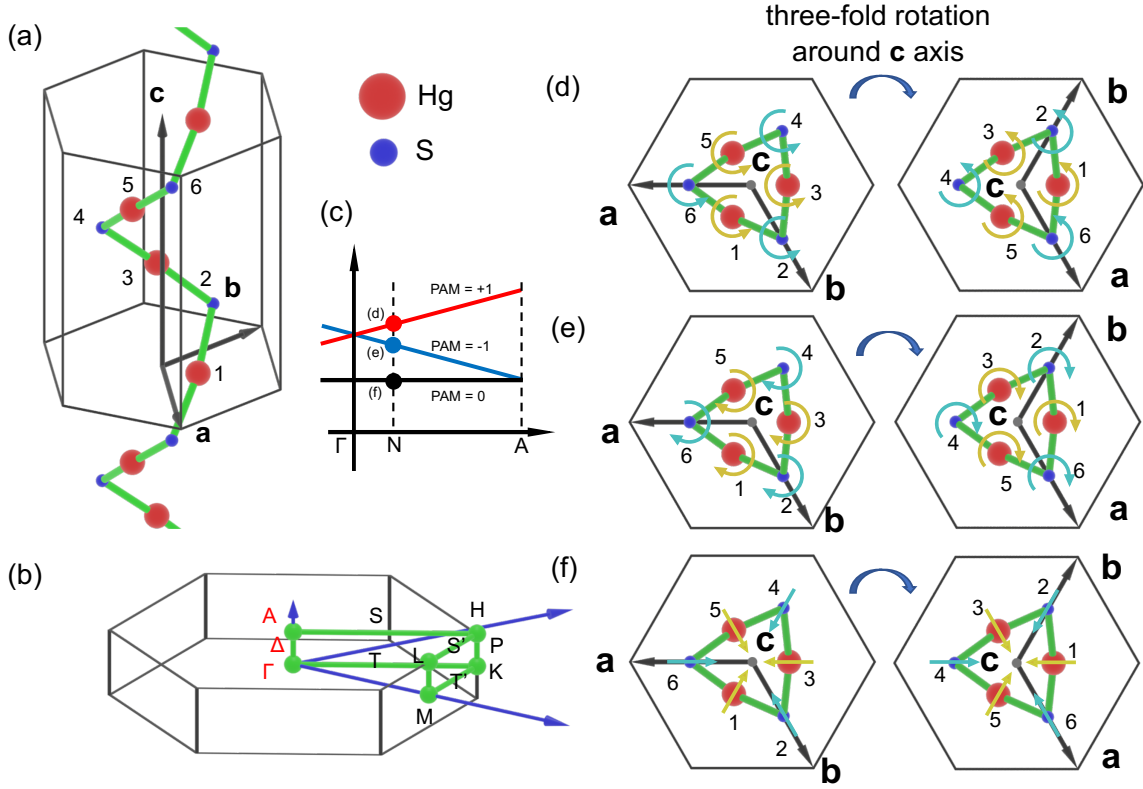


Figure 1: **Chiral properties of α -HgS.** (a) Right-handed helical chain along the c -axis of R-HgS. Each Hg atom (red sphere) is bonded with two S atoms (blue spheres). Chemical bonds are denoted as green lines. (b) Brillouin zone of α -HgS. (c) Schematic diagram of phonon dispersion from Γ to A point. The red, blue, and black circles at the N point correspond to the phonon modes of panels (d), (e), and (f), respectively. Two-dimensional projections of schematic atomic motions in R-HgS at point N for (d) a Δ_2 mode with $l_{\text{PAM}}^s = +1$, $l_{\text{AM}} > 0$, (e) a Δ_3 mode with $l_{\text{PAM}}^s = -1$, $l_{\text{AM}} < 0$, and (f) a Δ_1 mode with $l_{\text{PAM}}^s = 0$ and $l_{\text{AM}} \simeq 0$. Counter clockwise, clockwise circular, and linear motions indicate that l_{AM} is positive, negative, and zero, respectively. The three-fold rotation symmetry operation generates phase factors of atomic motions, namely, PAM l_{PAM}^s . The phase difference at the position of each atom after the operation is shown.

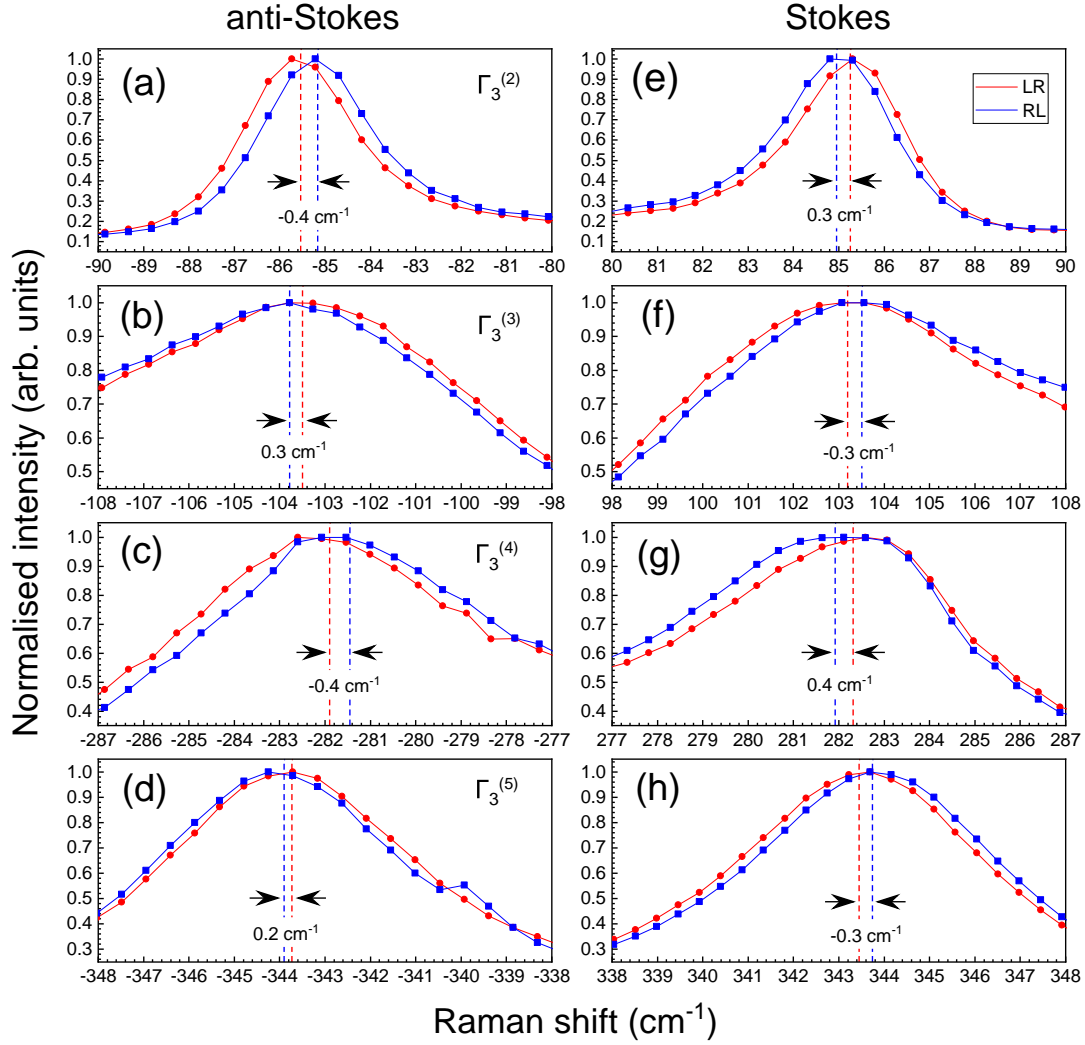


Figure 2: **Raman spectra of R-HgS.** (a–d) Anti-Stokes and (e–h) Stokes spectra of the Γ_3 modes. The black and red lines denote the Γ_3 modes experimentally observed with RL- and LR-polarised configurations, respectively. The values of the Γ_3 doublet splittings are shown in each figure.

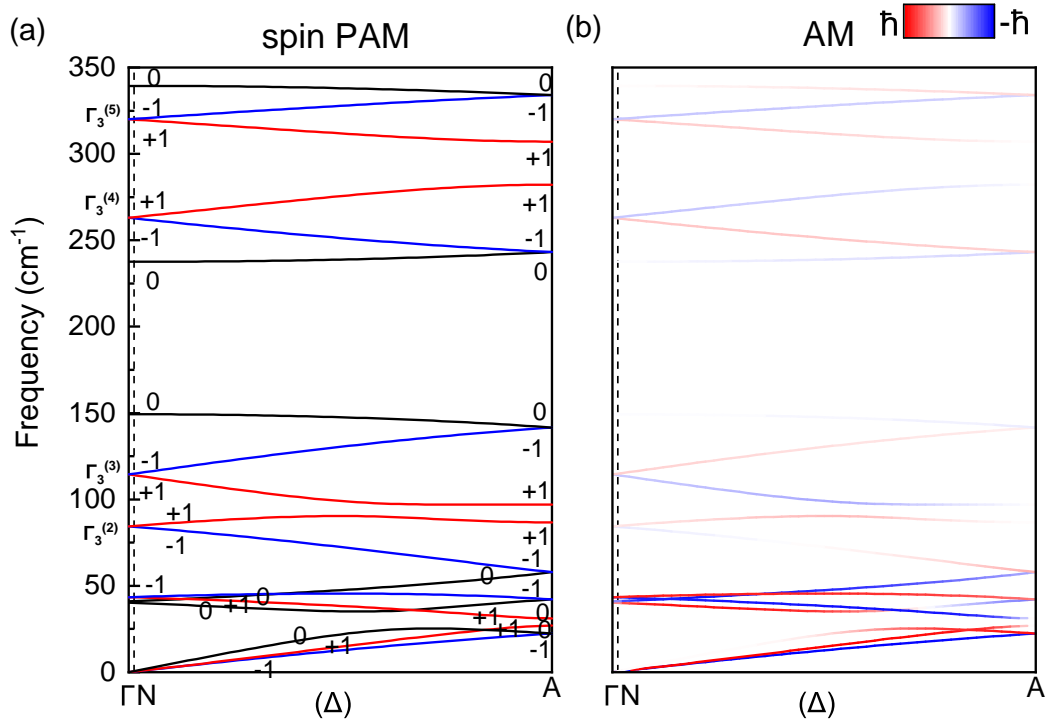
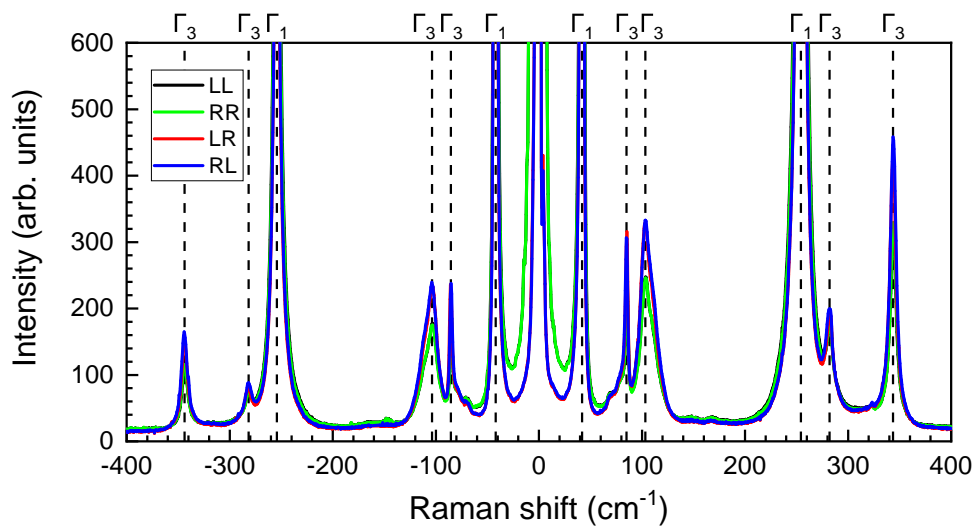
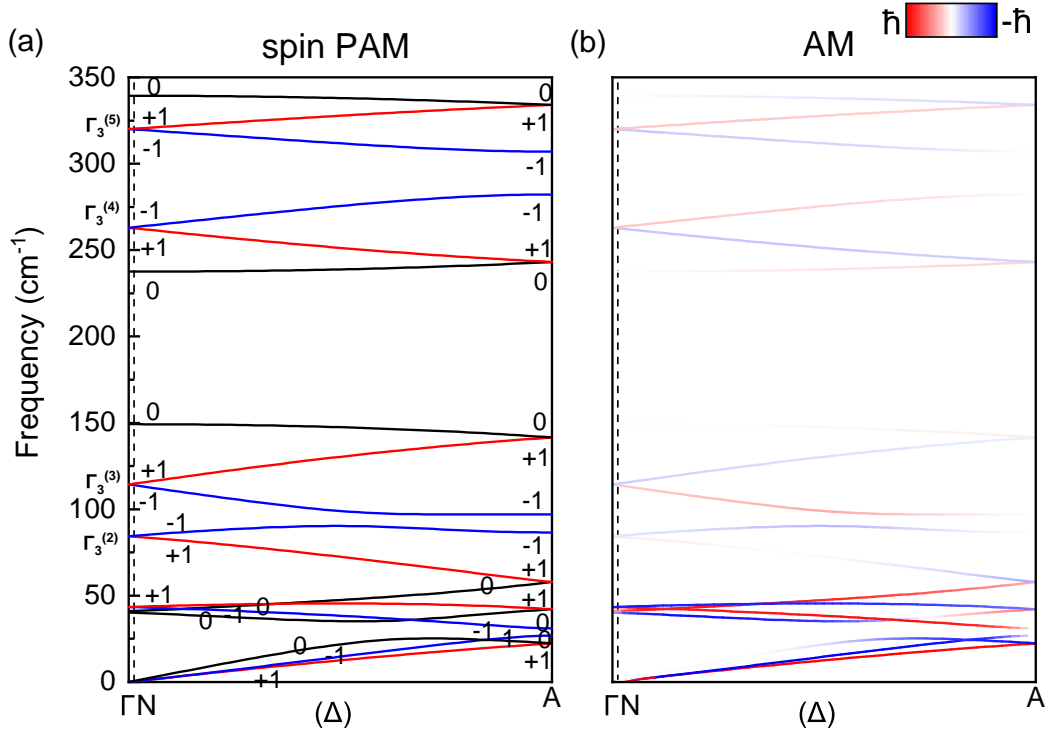


Figure 3: **Phonon dispersion curve of R-HgS along the right-handed helical axis.** (a) Black, red, and blue curves correspond to spin PAM $l_{\text{PAM}}^s = 0, +1, -1$, respectively. The wavenumbers at the N and A points are in the ratio of 1 : 80. (b) Phonon AM, denoted by the colour gradient. The red and blue curves correspond to the positive and negative AM, respectively.

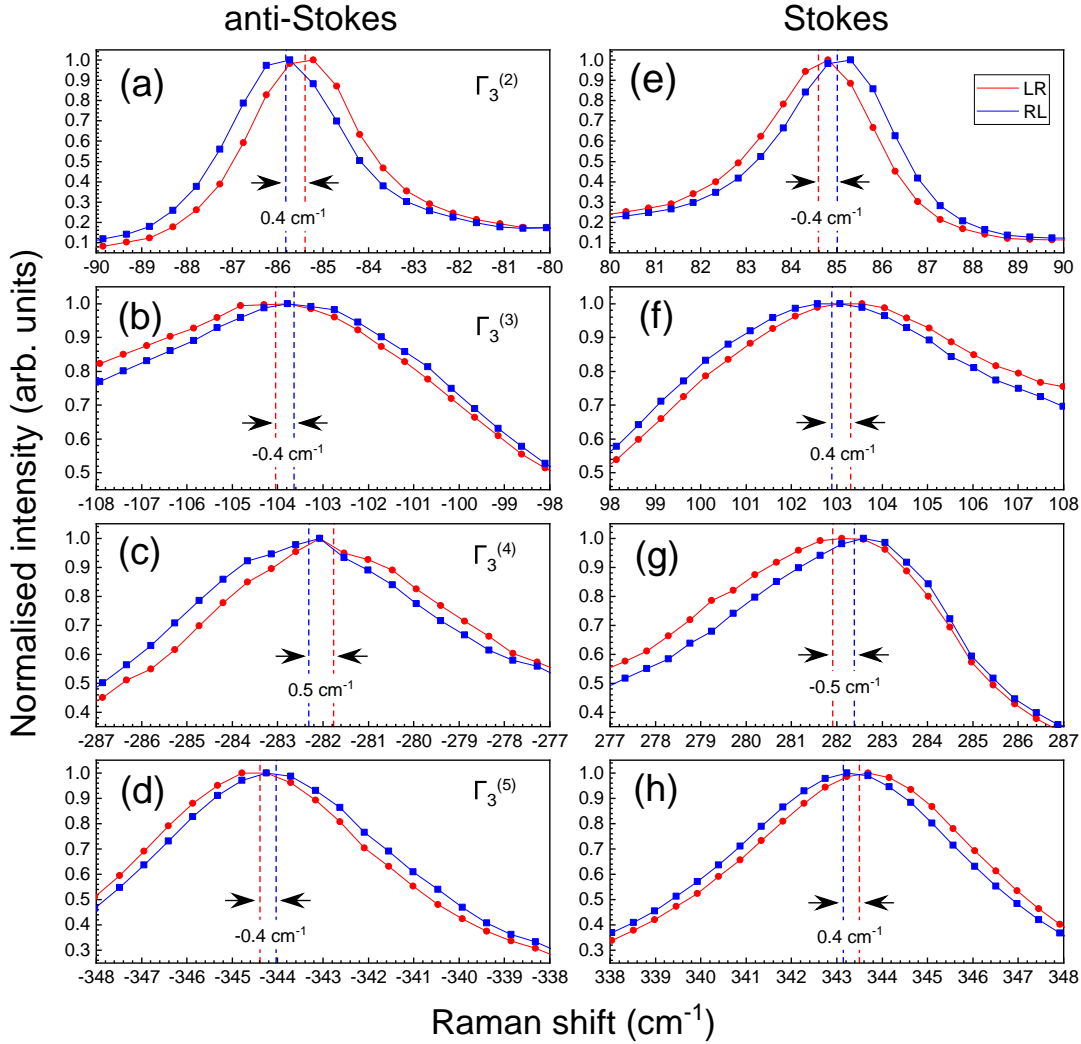


Extended Data Fig. 1 | Full Raman spectra of R-HgS. Full Raman spectra were recorded at room temperature using various polarised configurations. The black, green, red, and blue spectra represent the LL-, RR-, LR-, and RL-polarised configurations, respectively. R and L represent the right- and left-handed helicities of circularly polarised light, respectively.



Extended Data Fig. 2 | Phonon dispersion curve of L-HgS along the left-handed helical axis.

(a) The black, red, and blue curves correspond to spin PAM $l_{\text{PAM}}^s = 0, +1, -1$, respectively. (b) Phonon AM, denoted by the colour gradient. The red and blue curves correspond to the positive and negative AM, respectively.



Extended Data Fig. 3 | Raman spectra of α -HgS with unknown chirality. (a–d) Anti-Stokes and (e–h) Stokes spectra of the Γ_3 modes. The black and red lines denote the Γ_3 modes experimentally observed with RL- and LR-polarised configurations, respectively. R and L represent the right- and left-handed helicities of circularly polarised light, respectively. The values of the Γ_3 -doublet splittings are shown in each figure.

Extended Data Table 1 | phonon frequencies in α -HgS. The experimental values in cm^{-1} were obtained at room temperature. The calculated values in cm^{-1} are at the Γ point.

| Symmetry | Our experiments | Experiments ¹⁰ | Our calculations | Calculations ¹⁶ |
|------------------------------|-----------------|---------------------------|------------------|----------------------------|
| $\Gamma_{2,\text{LO}}^{(1)}$ | Inactive | | 40.2 | 44.1 |
| $\Gamma_1^{(1)}$ | 42 | 45 | 41.0 | 39.1 |
| $\Gamma_{3,\text{TO}}^{(1)}$ | | | 43.5 | 42.0 |
| $\Gamma_{3,\text{TO}}^{(2)}$ | 85 | 88 | 84.4 | 83.1 |
| $\Gamma_{3,\text{TO}}^{(3)}$ | 103 | 106 | 114.4 | 121.4 |
| $\Gamma_{2,\text{LO}}^{(2)}$ | Inactive | | 149.4 | 159.6 |
| $\Gamma_1^{(2)}$ | 254 | 256 | 237.5 | 232.1 |
| $\Gamma_{3,\text{TO}}^{(4)}$ | 282 | 283 | 263.0 | 259.3 |
| $\Gamma_{3,\text{TO}}^{(5)}$ | 344 | 345 | 320.2 | 319.2 |
| $\Gamma_{2,\text{LO}}^{(3)}$ | Inactive | | 339.4 | 337.7 |

Extended Data Table 2 | Chiral properties of phonons in R-HgS along the right-handed helical axis. Owing to the roughness of the sample surface, multiple splitting measurements were conducted, with the deviation indicated by the error bars.

| Symmetry at Γ point | Experiment | | | Calculation | | | | |
|----------------------------|------------|-------------------------------|-------------------------------|---------------------|-------------------------------|-------------------------------|-----------------------------|-----------------|
| | Config. | Frequency [cm ⁻¹] | Splitting [cm ⁻¹] | Symmetry at N point | Frequency [cm ⁻¹] | Splitting [cm ⁻¹] | $l_{\text{PAM}}^{\text{S}}$ | l_{AM} |
| $\Gamma_3^{(2)}$ | RL | 84.9 | 0.3 ± 0.01 | $\Delta_3^{(2)}$ | 84.2 | 0.4 | -1 | - |
| | LR | 85.3 | | $\Delta_2^{(2)}$ | 84.6 | | +1 | + |
| $\Gamma_3^{(3)}$ | LR | 103.2 | 0.3 ± 0.16 | $\Delta_2^{(3)}$ | 114.0 | 0.9 | +1 | - |
| | RL | 103.5 | | $\Delta_3^{(3)}$ | 114.9 | | -1 | + |
| $\Gamma_3^{(4)}$ | RL | 281.9 | 0.4 ± 0.08 | $\Delta_3^{(4)}$ | 262.7 | 0.7 | -1 | + |
| | LR | 282.3 | | $\Delta_2^{(4)}$ | 263.4 | | +1 | - |
| $\Gamma_3^{(5)}$ | LR | 343.5 | 0.3 ± 0.05 | $\Delta_2^{(5)}$ | 320.0 | 0.4 | +1 | + |
| | RL | 343.7 | | $\Delta_3^{(5)}$ | 320.4 | | -1 | - |

Extended Data Table 3 | Chiral properties of phonons in α -HgS with unknown chirality. The error bars take into account that multiple splitting measurements were conducted in the experiment, owing to the roughness of the sample surface. Calculations were performed for L-HgS.

| Symmetry at Γ point | Experiment | | | Calculation | | | | |
|-------------------------------|------------|----------------------------------|----------------------------------|------------------------|----------------------------------|----------------------------------|-----------------------------|-----------------|
| | Config. | Frequency [cm ⁻¹] | Splitting [cm ⁻¹] | Symmetry at N point | Frequency [cm ⁻¹] | Splitting [cm ⁻¹] | $l_{\text{PAM}}^{\text{S}}$ | l_{AM} |
| $\Gamma_3^{(2)}$ | LR | 84.6 | 0.4 ± 0.04 | $\Delta_3^{(2)}$ | 84.2 | 0.4 | +1 | + |
| | RL | 85.0 | | $\Delta_2^{(2)}$ | 84.6 | | -1 | - |
| $\Gamma_3^{(3)}$ | RL | 102.9 | 0.4 ± 0.04 | $\Delta_2^{(3)}$ | 114.0 | 0.9 | -1 | + |
| | LR | 103.3 | | $\Delta_3^{(3)}$ | 114.9 | | +1 | - |
| $\Gamma_3^{(4)}$ | LR | 281.9 | 0.5 ± 0.08 | $\Delta_3^{(4)}$ | 262.7 | 0.7 | +1 | - |
| | RL | 282.4 | | $\Delta_2^{(4)}$ | 263.4 | | -1 | + |
| $\Gamma_3^{(5)}$ | RL | 343.1 | 0.4 ± 0.03 | $\Delta_2^{(5)}$ | 320.0 | 0.4 | -1 | - |
| | LR | 343.5 | | $\Delta_3^{(5)}$ | 320.4 | | +1 | + |